

*To appear in the October 1995 Astronomical Journal*

## The Distribution of Column Densities and $b$ Values in the Lyman-Alpha Forest

Esther M. Hu<sup>1</sup>, Tae-Sun Kim<sup>1</sup>, Lennox L. Cowie<sup>1</sup>, and Antoinette Songaila<sup>1</sup>  
 Institute for Astronomy, University of Hawaii, 2680 Woodlawn Dr., Honolulu, HI 96822  
 hu@ifa.hawaii.edu, tsk@ifa.hawaii.edu, cowie@ifa.hawaii.edu, acowie@ifa.hawaii.edu

and

Michael Rauch  
 Observatories of the Carnegie Institution of Washington, 813 Santa Barbara St., Pasadena,  
 CA 91101  
 mr@ociw.edu

### ABSTRACT

We describe the properties of the Ly $\alpha$  forest in the column density range  $N_{\text{HI}} \geq 2 \times 10^{12} \text{ cm}^{-2}$  based on 1056 lines in the wavelength range 4300 – 5100 Å measured in extremely high S/N,  $R = 36,000$  spectra of four quasars. The column density distribution is well described by a  $-1.5$  power law to  $2 \times 10^{12} \text{ cm}^{-2}$ , below which limit confusion becomes too severe to measure a spectrum of individual clouds. The distribution of  $b$  values shows a well-defined lower envelope with a cutoff at  $b = 20 \text{ km s}^{-1}$  corresponding to a cloud temperature of 24,000 K. There is only a very small fraction (less than 1%) of narrow line clouds which cannot be identified with metal-lines. From modeling the Ly $\alpha$  absorption lines as complexes of clouds each with thermal broadening corresponding to  $b_c$  we find the  $b$  distribution can be understood if there is a mean of 3.25 clouds per absorption line with a spread in velocity centroids characterized by a dispersion of  $10.75 \text{ km s}^{-1}$ .

*Subject headings:* cosmology: early universe — cosmology: observations — galaxies: intergalactic medium — galaxies: quasars: absorption lines — galaxies: quasars: individual (0014+813 = S5 0014+81) — galaxies: quasars: individual (0302–003) — galaxies: quasars: individual (0636+680 = S4 0636+68) — galaxies: quasars: individual (0956+122)

---

<sup>1</sup>Visiting Astronomer, W. M. Keck Observatory, jointly operated by the California Institute of Technology and the University of California.

## 1. Introduction

The rich spectrum of Lyman-alpha absorption lines in quasars (generally known as the Lyman forest) was first noted by Lynds (1971) and studied in detail by Sargent *et al.* (1980). Because of its ubiquity and spatial correlation properties it is usual to assume that the forest is a distributed intergalactic population rather than being associated with large galaxies. In the first paper of the present series (Cowie *et al.* 1995) we analyzed the metallicity of the Lyman forest in clouds with column densities  $N_{\text{HI}} \sim 3 \times 10^{14} \text{ cm}^{-2}$  and found that these objects have average metallicities of approximately  $10^{-2}$  solar and consist of blends of much narrower components. In the present paper we turn to an analysis of the structure of lower column density forest clouds which, of necessity, must be based on studies of the Lyman absorption lines themselves since we do not currently have the sensitivity to detect metal lines in these objects.

Profile fitting to high resolution spectra has been used to study the velocity width (Doppler parameter  $b$ ) and the neutral hydrogen column densities  $N$  of the clouds. The distribution of Doppler parameters for the Ly $\alpha$  forest was found to peak near  $30 \text{ km s}^{-1}$  with a rather large spread from  $10$  to  $45 \text{ km s}^{-1}$  (Carswell *et al.* 1984; Atwood *et al.* 1985; Carswell *et al.* 1987). Subsequently, on the basis of the very high resolution echelle observations which had become possible by the end of the 1980's Pettini *et al.* (1990) claimed a tight correlation between  $b$  and  $N$  with many clouds having narrow profiles, leading to a median Doppler parameter of only  $17 \text{ km s}^{-1}$ . This result created understandable excitement in theoretical circles since it seemed to question the standard picture of the intergalactic matter confined in warm, extended, highly ionized gas clouds rather than small, cool, almost neutral entities. However, work by Carswell *et al.* (1991) using an identical observational setup did not confirm the Pettini *et al.* conclusions. In a recent detailed analysis Rauch *et al.* (1993) showed that the profile fitting methodology is sensitive to noise and that this can produce the results seen by Pettini *et al.*

The advent of the 10 m telescopes has resulted in an enormous improvement in the S/N which can be achieved in high resolution spectra of the faint quasars and in the present paper we discuss the distribution of low column density forest clouds and the  $b - N$  relationship based on such data obtained with the HIRES spectrograph on the Keck telescope. We find that the  $b$  distribution is quite invariant as a function of column density and that there is a sharp cutoff in the number of clouds below a value of about  $b_c = 20 \text{ km s}^{-1}$ , corresponding to temperature  $T = 24,000 \text{ K}$  for thermal broadening. We then argue that the broader absorption lines are blends of components, each with thermal broadening  $b_c$ , and each broad line having an average of 3.25 components and a velocity dispersion of  $10.75 \text{ km s}^{-1}$ . This

structure agrees with that found from the metal lines in the absorption systems just above the present column density range.

## 2. Data

As part of a program to measure (D/H) ratios in high- $z$  absorption systems, a number of bright ( $V < 18$ )  $z \sim 3$  quasars with partial Lyman-limit edges (optical depth  $\tau < 3.5$ ) have been observed with the HIRES spectrograph (Vogt *et al.* 1994) on the Keck 10 m telescope. A more complete description of the data and data reduction procedures is given in Songaila (1995). Each observation consists of a 3–6 hr exposure covering the wavelength range  $3600 \text{ \AA} \rightarrow 6000 \text{ \AA}$  at a resolution  $R$  of 36,000. The wavelength coverage is complete at shorter wavelengths ( $\lambda \lesssim 5000 \text{ \AA}$ ), but has small interorder gaps at longer wavelengths. Four of these spectra (toward the quasars 0014+813, 0302–003, 0636+680, and 0956+122) are well suited to a study of the low column-density ( $N_{\text{HI}} \sim 10^{12} - 10^{14} \text{ cm}^{-2}$ ) Ly $\alpha$  forest lines since they have good S/N ( $\gtrsim 50$  per resolution element) and fully cover the wavelength range between the quasar Ly $\alpha$  and Ly $\beta$  lines. The properties of the quasars are summarized in Table 1.

For each of these four quasars a  $600 \text{ \AA}$  region of wavelength space was chosen which lies above the wavelength at which Ly $\beta$  would enter the spectrum but well below the quasar Ly $\alpha$  emission wavelength to avoid proximity effects. The wavelength intervals are summarized in Table 1. The blaze function of the spectrograph in each order was removed by normalizing to fits to white dwarf standard stars obtained in the same configuration before and after each quasar observation. The continuum level of the spectrum was then established by an iterative fit to each spectral order: all points above a critical value were fitted by a third-order polynomial and renormalized; the critical value was then raised until the extrema in the noise in the Lyman forest region were matched to the extremal noise characteristics in the region above the rest-frame Lyman alpha emission taking into account the system response determined from the white dwarf observations and the overall spectral shape of the quasar. The normalized spectra were then spliced together to form a total spectrum. Each spectrum was fitted with an automatic Voigt-profile fitting procedure which added lines at each minimum in the spectrum where the average absorption depth per resolution element,  $\tau$ , exceeded 0.05, until a satisfactory fit was achieved, in which the residuals were consistent with the expected noise levels. A sample region of a spectrum with the fits and residuals is shown in Fig. 1. There were 1056 lines found with  $N_{\text{HI}} \geq 2 \times 10^{12} \text{ cm}^{-2}$ . The number of detected lines for each quasar is given in Table 1 together with the median  $b$  values in two column density ranges. The complete line catalogs and spectra are given in the Appendix.

For Q0014+813 we compared the detected clouds in detail with Rauch *et al.*'s (1992) profile fitting analysis of this quasar based on lower resolution ( $23 \text{ km s}^{-1}$ ) and lower S/N data. The agreement was generally good and almost always within Rauch *et al.*'s error estimates for both  $b$  and  $N$ . Almost all of the narrow lines in Rauch *et al.*'s sample are found to be caused by scatter, which is consistent with their prediction.

We have limited our primary analysis to the intermediate column density range  $2 \times 10^{12} \text{ cm}^{-2} < N_{\text{HI}} < 3 \times 10^{14} \text{ cm}^{-2}$  where uncertainties due to saturation are small. Measured column densities at  $N_{\text{HI}} > 3 \times 10^{14} \text{ cm}^{-2}$  are highly uncertain, but there are 66 clouds in the wavelength range with  $N_{\text{HI}} \geq 3 \times 10^{14} \text{ cm}^{-2}$ .

A plot of the  $b$  values of the fitted lines vs. column densities is shown in Fig. 2 for  $N_{\text{HI}}$  in the range  $3 \times 10^{12} \text{ cm}^{-2}$  to  $3 \times 10^{14} \text{ cm}^{-2}$ . The lower limit is chosen to avoid the optical depth selection effect against shallow lines, which is illustrated in Fig. 2 by the solid line, which corresponds to  $\tau \sim 0.05$ , and to minimize noise artifacts in the profile fitting. We have separated Q0636+680 (Fig. 2a), which has a relatively large number of narrow lines, from Q0014+813, Q0302–003, and Q0956+122, which have relatively few narrow lines. In Q0636+680 17 of the 266 lines in the  $3 \times 10^{12} \text{ cm}^{-2} \leq N_{\text{HI}} \leq 3 \times 10^{14} \text{ cm}^{-2}$  range have  $b < 14 \text{ km s}^{-1}$ . A detailed analysis of these narrow lines (Table 2) shows that 13 of these can straightforwardly be identified as metal lines based on their correspondance to a strong Ly $\alpha$  line and to other narrow lines in the spectrum. The remaining narrow lines are quite likely to be unidentified metal lines. However, the most important point to draw from Q0636+680 is that narrow lines can easily be retrieved from the spectrum if they are present, and that the absence of large numbers of narrow lines in the three other quasars is not a selection effect. The ease with which narrow lines can be picked out is also illustrated in Fig. 1.

For Q0014+813, Q0302–003, and Q0956+122 (Fig. 2b) there are only 11 out of 670 clouds with  $3 \times 10^{12} \text{ cm}^{-2} \leq N_{\text{HI}} \leq 3 \times 10^{14} \text{ cm}^{-2}$  which have  $b < 14 \text{ km s}^{-1}$ . Eight of these are straightforwardly identified as metal lines (Table 2). Thus less than 1% of the Ly $\alpha$  forest clouds have  $b < 14 \text{ km s}^{-1}$ .

The  $b - N$  distribution of Fig. 2b has a fairly well defined lower envelope which we have outlined with the dotted line  $b = 16 \text{ km s}^{-1} + 4(N_{\text{HI}}/10^{14} \text{ cm}^{-2}) \text{ km s}^{-1}$ . As we shall show in Fig. 3 the slope in this lower extremum is primarily an artifact of the much larger number of clouds at lower  $N_{\text{HI}}$  and the increased scatter in the  $b$  determinations, and the distribution is consistent with a sharp cutoff below  $b = 20 \text{ km s}^{-1}$  which is invariant with column density.

Turning to the distribution of column densities we show the raw distribution of counts per unit column density and  $z$ ,  $\left(\frac{dn}{dN dz}\right)$ , for the four quasars in Fig. 3. The counts are

indistinguishable within the Poisson uncertainties, indicating that the properties of the forest are highly invariant and that the retrieval of the lines is reproducible from system to system.

### 3. Analysis

In analyzing the data of §2 it is necessary to deal with the problems of blending and selection since confusion becomes significant at the low column density end. Because there are a very large number of weak clouds the probability of cloud blending is high and can result in substantial incompleteness in the low column density counts and widening of the  $b$  value distribution. Very faint clouds may also be lost if their  $b$  values are too large and their central optical depths are too low compared to the noise levels. This latter selection effect, which is relatively unimportant at  $N_{\text{HI}} > 3 \times 10^{12} \text{ cm}^{-2}$ , is illustrated by the solid line in Fig. 2.

In order to remove these effects we have performed a number of simulations to measure the cloud incompleteness and  $b$  distribution widening as a function of column density. In these simulations we assumed that the distribution of column densities was described by a  $-1.5$  power law normalized to produce the observed number of lines, and that the distribution of  $b$  values was described by a Gaussian with  $\bar{b} = 28 \text{ km s}^{-1}$  and  $\sigma(b) = 10 \text{ km s}^{-1}$  truncated below  $b = 20 \text{ km s}^{-1}$ . We also assumed that the  $z$  distributions were uncorrelated. These input parameters were chosen to produce output spectra which closely match the observed spectra. Artificial spectra were generated and convolved with the instrumental spectral response with the appropriate Gaussian noise added. The finding program was then run on these artificial spectra to obtain lists of clouds.

The completeness of the cloud recovery in the artificial spectra is tabulated in Table 3. Above  $10^{13} \text{ cm}^{-2}$  essentially all clouds are recovered, together with a small number of blends of lower column density clouds, but below this column density the cloud recovery rate drops, falling to a completeness of only 25% in the interval  $N_{\text{HI}} = 2 \times 10^{12} \text{ cm}^{-2} \rightarrow 4 \times 10^{12} \text{ cm}^{-2}$ . It is important to emphasize that this effect is not determined by the S/N since the incompleteness is almost wholly dominated by confusion: the recovery rate is essentially the same for an artificial spectrum with infinite S/N.

The number of clouds per unit  $z$  and unit  $N_{\text{HI}}$  in the observed spectra is shown in Fig. 3 before and after correcting for the incompleteness. The corrected distribution in the range  $2 \times 10^{12} - 3 \times 10^{14} \text{ cm}^{-2}$  is well fit by a power law of the form  $N^{-\beta}$  where  $N$  is the HI column density. The best fit to the power law index  $\beta$  is  $-1.46$  with a 95% confidence range of  $(-1.37 \rightarrow -1.51)$ .

Remarkably, the power law exponent of the spectrum fitted over this limited column density agrees well with the power law fit determined over much larger  $N_{\text{HI}}$  ranges (Tytler 1987, Sargent *et al.* 1989). In Fig. 4 we have compared the present data with Petitjean *et al.*'s (1993) summary of recent data at higher column densities and with a power law fit with  $\beta = -1.46$ . For consistency with their notation Fig. 4 shows the quantity

$$f(N) = \frac{m}{\Delta N \sum \Delta X} \quad (1)$$

where  $m$  is the number of clouds in the intervals  $dX$  and  $dN$  with  $X \equiv 0.5[(1+z)^2 - 1]$ .  $f(N)$  is roughly a factor of 3.8 less than  $\left(\frac{dn}{dN dz}\right)$ .  $\sum \Delta X = 7.37$  for the present sample. We have tabulated  $f(N)$  in Table 3 for the present data. The two data sets agree extremely well in the overlap region. The present data set may also be used to check Petitjean *et al.*'s finding that there is a significant deficit of clouds in the range  $10^{15} - 10^{17} \text{ cm}^{-2}$  compared to the power law extrapolation from higher and lower column densities. The best power law fit to  $f(N)$  in the regime  $2 \times 10^{12} - 3 \times 10^{14} \text{ cm}^{-2}$ , given by

$$f(N) = 4.9 \times 10^7 N^{-1.46} \quad (2)$$

with all quantities expressed in cgs units, would predict 193 clouds with  $N_{\text{HI}} > 3 \times 10^{14} \text{ cm}^{-2}$  compared to the 70 observed, implying that there is indeed a significant deficit between  $3 \times 10^{14} \text{ cm}^{-2}$  and  $10^{17} \text{ cm}^{-2}$ . Setting  $\beta = -1.51$  only reduces the predicted number of clouds to 127. Thus there is indeed a significant steepening of the slope above  $N_{\text{HI}} = 3 \times 10^{14} \text{ cm}^{-2}$ .

The key issues for the  $b - N$  distribution is whether the rise of the lower envelope in  $b$  with  $N$  is real and whether there are any clouds with very large  $b$  or whether these are primarily random blends. We have compared the observed distribution of  $b$  values in the high ( $N_{\text{HI}} = 3 \times 10^{13} - 3 \times 10^{14} \text{ cm}^{-2}$ ) and low ( $N_{\text{HI}} = 3 \times 10^{12} - 3 \times 10^{13} \text{ cm}^{-2}$ ) column density regimes in Fig. 5. The models give an acceptable fit to both distributions, showing that a single cutoff at  $b = 20 \text{ km s}^{-1}$  can be adopted at all column densities. A better fit is given by adopting  $b = 18 \text{ km s}^{-1}$  in the regime  $3 \times 10^{12} - 3 \times 10^{13} \text{ cm}^{-2}$  and  $b = 22 \text{ km s}^{-1}$  in the  $3 \times 10^{13} - 3 \times 10^{14} \text{ cm}^{-2}$  range, so a weak increase in the cutoff  $b$  with  $N$  may be slightly favored but is not required. The drop in  $b$  with decreasing  $N$  may occur because weaker lines are more susceptible to having their Doppler parameters underestimated, due to the finite signal-to-noise of the data.

#### 4. Discussion

Our first observational conclusion is that the number of Ly $\alpha$  forest clouds rises as a smooth  $\beta = -1.5$  power law in the range  $2 \times 10^{12} - 3 \times 10^{14} \text{ cm}^{-2}$  and shows no sign of

turnover at the low column density end. Confusion makes it essentially impossible to extend this result to much lower column densities. The second result is that the forest clouds have a well defined lower envelope to the  $b$  values of  $b = 20 \text{ km s}^{-1}$ . It is possible for this limit to have a weak dependence on column density rising from  $b = 18 \text{ km s}^{-1}$  at  $3 \times 10^{12} - 3 \times 10^{13} \text{ cm}^{-2}$  to  $b = 22 \text{ km s}^{-1}$  at  $3 \times 10^{13} - 3 \times 10^{14} \text{ cm}^{-2}$ , but this is not required by the data. The distribution of  $b$  values can be adequately described by a Gaussian with  $\bar{b} = 28 \text{ km s}^{-1}$  and a  $\sigma(b) = 10 \text{ km s}^{-1}$  truncated below  $b = 20 \text{ km s}^{-1}$  at all measured column densities.

The mean intergalactic density,  $n$ , contributed by the clouds with these column densities may be obtained by integrating equation (2) whence

$$n = \frac{H_0}{c} (1+z)^3 (1+2q_0z)^{\frac{1}{2}} \int_{N_{min}}^{N_{max}} \frac{f(N) N dN}{F(N)}. \quad (3)$$

Here  $F(N)$  is the mean ionization fraction at column density  $N$ . Assuming that  $F$  is not such a steep function of  $N$  that it weights the primary density contribution to the low column density end, we can integrate equation (3) to obtain

$$\Omega_b = \frac{1.5 \times 10^{-7}}{\langle F \rangle} \left( \frac{N_{max}}{3 \times 10^{14} \text{ cm}^{-2}} \right)^{0.54} \quad (4)$$

where  $F$  is the appropriately weighted mean value and we have adopted  $H_0 = 100 \text{ km s}^{-1} \text{ Mpc}^{-1}$  and  $q_0=0.5$ . The corresponding mean physical separation is

$$L = 120 \text{ kpc} \left( \frac{N_{min}}{2 \times 10^{12} \text{ cm}^{-2}} \right)^{0.46}. \quad (5)$$

As Press & Rybicki (1993) have emphasized, equation (4) shows at once that the larger  $b$  values cannot be caused by the thermal broadening in the most simple photoionization model where the clouds are in thermal equilibrium and have no kinematic broadening. Thus from Donahue & Shull (1991)

$$b = 28 \text{ km s}^{-1} U^{0.076} \quad (6a)$$

$$T = 4.9 \times 10^4 U^{0.152} \quad (6b)$$

$$F = 3.4 \times 10^{-6} U^{-1.066} \quad (6c)$$

in terms of their ionization parameter  $U$ . However, from equation (4) we see that  $\langle F \rangle$  must be greater than  $1.1 \times 10^{-5}$  in order not to exceed the baryon limit from nucleosynthesis of 0.01 (Walker *et al.* 1991) and hence  $U < 0.3$  implying  $b < 25 \text{ km s}^{-1}$ .

The structure of the C IV lines at slightly higher column densities (Cowie *et al.* 1995) suggests an alternative picture. If we assume instead that each cloud is a blend of comparable

column density components and that the observed  $b$  value is produced by this blend of components each with a thermally broadened  $b_c$  and a centroid velocity spread described by  $f(v_c)$ , then the value  $b_c$  must be identified with the lower cutoff in  $b$  which will occur when an absorption line is dominated by a single component. This model is simplistic in assuming that all components have similar column densities and that there is a single thermal broadening for the clouds when in fact there are likely to be density and ionization parameter variations from component to component. However, the use of a single value for  $b$  is justified by the extremely weak dependence of  $b$  on  $U$  in equation (6). Conversely, the extremely weak dependence of  $b_c$  on  $U$  also implies that  $U$  and  $F$  can be determined only to order of magnitude. Thus for  $b_c = 20 \text{ km s}^{-1}$ ,  $U = 10^{-2}$  and  $F = 3.8 \times 10^{-4}$ , while for  $b_c = 18 \text{ km s}^{-1}$ ,  $U = 10^{-2.5}$  and  $F = 1.7 \times 10^{-3}$ , and for  $b_c = 22 \text{ km s}^{-1}$ ,  $U = 10^{-1.4}$  and  $F = 10^{-4}$ . However, and very reassuringly, this agrees with the  $U$  of  $10^{-2} \rightarrow 10^{-1.5}$  estimated by Cowie *et al.* (1995) based on the ionization balance in clouds just above  $N_{\text{HI}} = 3 \times 10^{14} \text{ cm}^{-2}$ . Furthermore, the hydrogen thermal broadening would predict a thermal  $b$  value of  $6 \text{ km s}^{-1}$  for carbon lines, which is very close to the value of  $7 \text{ km s}^{-1}$  found by Cowie *et al.* Finally, with  $F = 3 \times 10^{-4}$ , then  $\Omega_b = 5 \times 10^{-4}$  and very roughly 4% of the baryons inferred from nucleosynthesis lie in these components. Thus this model appears to provide a self-consistent description.

We can determine the average number of components and their velocity spread by comparing the predicted spread in  $b$  values with the observed distribution. If we assume that each absorption line consists of a number of components  $n$ , each thermally broadened with  $b_c = 20 \text{ km s}^{-1}$  and described by the probability distribution

$$P(n) \sim \frac{1}{n!} (N)^n \quad \text{with } n \geq 1 \quad (7)$$

and that the centroids of these velocity components are described by a Gaussian velocity distribution function characterized by  $\sigma(v_c)$ , then we can model the observed  $b$  value distribution function to determine  $N$  and  $v_c$ . We find that these quantities are extremely tightly constrained with a best fit of  $N=3.1$ , corresponding to a mean of 3.25 components per absorption line, and  $\sigma(v_c) = 10.75 \text{ km s}^{-1}$ . Any smaller value of  $N$  results in too many single component clouds with  $b = b_c$  while larger  $N$  result in a Gaussian spread of  $b$  values which is also a poor fit to the observed distribution. The velocity spread is slightly smaller than the value of  $18 \text{ km s}^{-1}$  found by Cowie *et al.* (1995) for the spread in C IV components in  $N_{\text{HI}} \geq 3 \times 10^{14} \text{ cm}^{-2}$  clouds and the mean number of C IV components (2.5) per absorption line systems is slightly smaller. This could represent a velocity dependent ionization effect or a difference between the column density samples, but most likely it is due to observational uncertainty and reflects the difficulty of measuring the C IV dispersion. The presently determined dispersion should be considerably more accurate.



At larger velocity separations the components are no longer blended and we may directly investigate the two-point correlation function in the form

$$\xi(v) = \frac{N_{pairs}(v)}{N_{pairs}^{art}(v)} - 1 \quad (8)$$

where  $N_{pairs}(v)$  is the number of observed pairs at separation  $v$  and  $N_{pairs}^{art}(v)$  is the number of expected pairs determined from the artificial spectra with no correlation. This is illustrated in Fig. 6. For the forest sample with  $7 \times 10^{12} \text{ cm}^{-2} < N_{\text{HI}} < 3 \times 10^{14} \text{ cm}^{-2}$  we find no evidence of correlation at  $v > 150 \text{ km s}^{-1}$  consistent with previous studies (Sargent *et al.* 1980) but for  $50 \text{ km s}^{-1} < v < 150 \text{ km s}^{-1}$  we do find a significant excess of  $0.17 \pm 0.045$  – slightly smaller than, but consistent with, the value of  $0.32 \pm 0.08$  found by Webb (1987). Intriguingly, if we divide the sample by column density the correlation increases with a value of  $0.73 \pm 0.13$  for  $4 \times 10^{13} < N_{\text{HI}} < 3 \times 10^{14} \text{ cm}^{-2}$  and  $0.21 \pm 0.07$  for  $7 \times 10^{12} < N_{\text{HI}} < 4 \times 10^{13} \text{ cm}^{-2}$  suggesting that clouds are preferentially correlated with clouds of similar density, and that there might be a weakening of the correlation as we move to lower column densities. Crofts (1989), Chernomordik (1995), and Cristiani *et al.* (1995) have previously noted such an effect. Cristiani *et al.* found a correlation with a value of  $0.89 \pm 0.18$  at  $\Delta v \leq 100 \text{ km s}^{-1}$  for  $N_{\text{HI}} \geq 6 \times 10^{13} \text{ cm}^{-2}$  clouds at slightly higher redshift in the spectrum of the quasar Q0055–269. For  $2 \times 10^{13} \text{ cm}^{-2} \leq N_{\text{HI}} \leq 6 \times 10^{13} \text{ cm}^{-2}$  they obtain  $0.38 \pm 0.1$ . These values are roughly consistent with the present results, and together they may suggest that the correlation function does weaken at lower column densities. Suggestions of anticorrelation features in the two-point correlation at a few to several hundred  $\text{km s}^{-1}$  may also be noted in Fig. 6. While we cannot be sure of the nature of this phenomenon, such features appear real. Inspection of figures 8 and 9 of Cristiani *et al.* (1995) shows that similar negative features are visible in the correlation function of their high column density sample,  $\log N_{\text{HI}} > 14$  (see also Meiksin & Bouchet 1995). Anticorrelation features are expected to occur when some Ly $\alpha$  clouds are forming velocity caustics during turnaround (Kaiser 1987; McGill 1990), but on smaller scales of a few hundred  $\text{km s}^{-1}$  they may be more likely to be due to gas dynamical effects like pressure fluctuations (Webb & Barcons 1991) or inhomogeneous ionization (Meiksin & Bouchet 1995).

Finally, we may combine the present data with the properties inferred from the metal lines in the  $N_{\text{HI}} = 3 \times 10^{14} \text{ cm}^{-2}$  Ly $\alpha$  forest to estimate the cloud properties. Cowie *et al.* (1995) found from the ionization balance in the metals that  $U = 10^{-2} \rightarrow 10^{-1.5}$  for  $N_{\text{HI}} = 3 \times 10^{14} \text{ cm}^{-2}$  clouds at this redshift, and, that the neutral hydrogen fraction was then  $4.6 \times 10^{-4} U_{-2}^{-1.066}$  (from Eq. 6(c) where  $U_{-2} \equiv U/10^{-2}$ ). By the definition of  $U$  the total density in the cloud is  $n_{tot} = 6.3 \times 10^{-3} J_{-21}/U_{-2}$  where  $J_{-21}$  is the incident ionizing intensity just above the Lyman edge in units of  $10^{-21} \text{ ergs cm}^{-2} \text{ s}^{-1} \text{ Hz}^{-1} \text{ sr}^{-1}$ . Assuming this ionization fraction holds over the relevant column density range, the line-of-sight cloud size,

$D = 10 \text{ pc } U_{-2}^{2.066} J_{-21}^{-1} (N_{\text{HI}}/10^{14} \text{ cm}^{-2})$ . This is  $10^{-5}$  to  $10^{-4}$  of the separation distance for  $N_{\text{HI}} = 10^{14} \text{ cm}^{-2}$ , suggesting that the filling factor of the forest clouds is correspondingly small. The physical dimensions are similarly small compared to the transverse dimensions (Bechtold *et al.* 1994; Dinshaw *et al.* 1994), suggesting that the clouds are highly flattened. (Rauch & Haehnelt 1994 give a more indirect argument to this effect.) The internal density represents an overdensity of  $1400 \left(\frac{\Omega_{\text{IGM}}}{0.01}\right)^{-1}$  with respect to the average IGM, where  $\Omega_{\text{IGM}}$  is the fraction of the closure density in baryons.

The internal kinematic structure strongly favors models in which the underlying formation mechanism is gravitational or kinematic such as the minihalo model of Rees (1986) or the pancake model of Cen *et al.* (1994). The objects are extremely elongated, which would seem to favor the latter model. These models allow a natural understanding of the kinematic structure and the spread of velocities, since higher infall or shock velocities would result in too high a temperature for neutral hydrogen to be present. Indeed, the pancake model produces a natural explanation for the number of components, since we will see the pancake itself, the outgoing shocks, and possibly the surrounding infalling material. In its current version the pancake model does not correctly predict the extrapolation of the power law distribution of column densities below  $10^{13} \text{ cm}^{-2}$  found in the present paper but this may be very much a function of the assumed details.

## APPENDIX

Plots and line lists for spectral line fits for Q0014+813, Q0302–003, Q0636+680, and Q0956+122. Each plot shows the normalized spectrum with overlying profile fits, plotted against vacuum heliocentric wavelength. Vertical tick marks indicate the positions of line features, with every tenth line numbered. Lines with  $N_{\text{HI}} \geq 3 \times 10^{12} \text{ cm}^{-2}$  and  $b < 14 \text{ km s}^{-1}$  are marked by the filled boxes. Residuals from the fits are plotted below each spectrum. A tabulation of the line identifications by wavelength, with  $b$  value, and redshift and column density (under the assumption that these are Ly $\alpha$  features) is given in Tables A1 and A2.

We would like to thank Jerry Ostriker, Jordi Miralda-Escudé, and Martin Haehnelt for very helpful discussions. These observations would not have been possible without Steve Vogt’s HIRES spectrograph.

## REFERENCES

- Atwood, B., Baldwin, J. A., & Carswell, R. F. 1985, *ApJ*, 292, 58
- Bechtold, J, Crofts, A. P. S., Duncan, R. C., & Fang, Y. 1994, *ApJ*, 437, L83
- Carswell, R. F., Lanzetta, K. M., Parnell, H. C., & Webb, J. K. 1991, *ApJ*, 371, 36
- Carswell, R. F., Morton, D. C., Smith, M. G., Stockton, A. N., Turnshek, D. A., & Weymann, R. J. 1984, *ApJ*, 278, 486
- Carswell, R. F., Webb, J. K., Baldwin, J. A., & Atwood, B. 1987, *ApJ*, 319, 709
- Cen, R., Miralda-Escudé, J., Ostriker, J. P., & Rauch, M. 1994, *ApJ*, 437, L9
- Cowie, L. L., Songaila, A., Kim, T.-S., & Hu, E. M. 1995, *AJ*, 109, 1522
- Chernomordik, V. V. 1995, *ApJ*, 440, 431
- Cristiani, S., D’Odorico, S., Fontana, A., Giallongo, E., & Savaglio, S. 1995, *MNRAS*, 273, 1016
- Crofts, A. P. S. 1989, *ApJ*, 336, 550
- Dinshaw, N., Impey, C. D., Foltz, C. B., Weymann, R. J., & Chaffee, F. H. 1994, *ApJ*, 437, L87
- Donahue, M., & Shull, J. M. 1991, *ApJ*, 383, 511
- Kaiser, N. 1987, *MNRAS*, 227, 1
- Lynds, R. 1971, *ApJ*, 164, L73
- McGill, C. 1990, *MNRAS*, 242, 428
- Meiksin, A., & Bouchet, F. R. 1995, *ApJ*, submitted
- Pettini, M., Hunstead, R. W., Smith, L. J., & Mar, D. P. 1990, *MNRAS*, 246, 545
- Petitjean, P., Webb, J. K., Rauch, M., Carswell, R. F., & Lanzetta, K. 1993, *MNRAS*, 262, 499
- Press, W. H., & Rybicki, G. B. 1993, *ApJ*, 418, 585
- Rauch, M., Carswell, R. F., Chaffee, F. H., Foltz, C. B., Webb, J. K., Weymann, R. J., Bechtold, J., and Green, R. F. 1992, *ApJ*, 390, 387
- Rauch, M., Carswell, R. F., Webb, J. K., & Weymann, R. J. 1993, *MNRAS*, 260, 589
- Rauch, M., & Haehnelt, M. G. 1995, to appear in the Proceedings of the ESO Workshop on QSO Absorption Lines, Nov. 21–24, 1994
- Rees, M. J. 1986, *MNRAS*, 218, 25P

- Sargent, W. L. W., Young, P. J., Boksenberg, A., & Tytler, D. 1980, *ApJS*, 42, 41
- Sargent, W. L. W., Steidel, C. C., & Boksenberg, A. 1989, *ApJS*, 69, 703
- Songaila, A. 1995, in preparation
- Tytler, D. 1987, *ApJ*, 321, 49
- Vogt, S. S., *et al.* 1994, *S.P.I.E.*, 2198, 362
- Walker, T. P., Steigman, G., Schramm, D. N., Olive, K. A., & Kang, H. S. 1991, *ApJ*, 376, 51
- Webb, J. K. 1987, in *Observational Cosmology*, Proc. of IAU Symposium No. 124, edited by A. Hewitt, G. Burbidge, and L. Z. Fang (Reidel, Dordrecht), p. 803
- Webb, J. K., & Barcons, X. 1991, *MNRAS*, 250, 270

Fig. 1.— A sample 50 Å region of the spectrum of Q0302–003 showing fits to identified lines overlaid upon the normalized spectrum. Residuals to the fits are shown below, and it can be seen that there are no systematic residuals associated with the profile fits. The wavelengths of each line are marked by ticks above the spectrum. There are two lines with  $b < 14 \text{ km s}^{-1}$  in this region of spectrum where the ticks are overlaid by boxes. These lines correspond to a C IV doublet at  $z = 1.8924$  (Table 2) and are easily distinguished from the broader forest lines. The number of lines fitted for each quasar is summarized in Table 1.

Fig. 2.— The distribution of components with respect to column density and  $b$  value for the quasar systems. Q0014+813, Q0302–003, and Q0956+122 have been plotted separately from Q0636+680, since the latter system has many narrow features known to correspond to metal lines. For each figure we have plotted only clouds with  $3 \times 10^{12} \text{ cm}^{-2} < N_{\text{HI}} < 3 \times 10^{14} \text{ cm}^{-2}$  shown by the dashed lines. Very broad clouds with low column densities and high  $b$  values will not be detected. The solid line shows this selection for  $\tau = 0.05$ , above which clouds should be easily found. We have attempted to identify all cloud with  $b \leq 14 \text{ km s}^{-1}$  as metal lines. Such narrow components that have been identified with metal line systems are indicated with a surrounding box. The dotted line shows, for Fig. 2b, the apparent lower bound to the  $b$  values of Ly $\alpha$  forest clouds. The boundary appears to be a real physical limit, and the plot of Q0636+680 shows that the fitting program is quite capable of picking out narrow components where these are present.

Fig. 3.— The raw and corrected distributions of counts per unit column density and redshift in the column density regime  $2 \times 10^{12} - 3 \times 10^{14} \text{ cm}^{-2}$ . Squares show the distribution for Q0636+680, diamonds for Q0302–003, asterisks for Q0014+813, and triangles for Q0956+122. The dashed line shows the average raw counts for all four quasars. It can be seen that the raw counts are indistinguishable from system to system, within the Poisson noise, and that both the properties of the Ly $\alpha$  forest and the capacity of the program to retrieve lines is highly invariant for all three quasars. The large open boxes show the column density distribution corrected for incompleteness with the best power law fit shown as a solid line.

Fig. 4.— Comparison of the cloud number distribution at low and high column densities. The data in the present survey, covering the column density range  $2 \times 10^{12} - 3 \times 10^{14} \text{ cm}^{-2}$ , are shown with filled squares, along with the best power-law fit ( $-1.46$ ) over this region. This fit has been extrapolated to higher column densities, and the higher column density data compiled by Petitjean *et al.* (1993) is shown with diamonds overlaid with the associated error bars. The deviations below the line around  $10^{15} - 10^{17} \text{ cm}^{-2}$  which were noted by Petitjean *et al.* are confirmed by the present data (see text). However, as was originally emphasized by Tytler (1987), the overall fit to a single power-law is remarkably good over nearly ten orders of magnitude in column density.

Fig. 5.— Comparison of the distribution of  $b$  values derived from the artificial spectra compared with the observed distributions. The lower left panel shows the input distribution for the artificial spectra averaged over eight realizations. In the right hand panels we show the recovered distributions (dashed lines) compared with the observed distributions (solid lines) in the high and low column density ranges. The observed distribution is the average for Q0014+813, Q0302-003, and Q0956+122 with known metal lines excluded.

Fig. 6.— The correlation functions vs. velocity separation in the column density ranges  $4 \times 10^{13} - 3 \times 10^{14} \text{ cm}^{-2}$  (upper graph) and  $7 \times 10^{12} - 4 \times 10^{13} \text{ cm}^{-2}$  (lower graph). The correlation functions have been computed in  $50 \text{ km s}^{-1}$  bins and the dotted line shows the  $1\sigma$  error computed from the number of artificial pairs.

Table 1. Fitted Quasars

Quasar	$m$ (1450 Å)	$z_{em}$	$\lambda\lambda$ (Å)	No. lines		Low $N$	High $N$
				$N > 2 \times 10^{12} \text{ cm}^{-2}$	$N > 3 \times 10^{14} \text{ cm}^{-2}$	Median $b$ (km s <sup>-1</sup> )	Median $b$ (km s <sup>-1</sup> )
Q0014 + 813	16.7	3.384	4500–5100	254	17	30	32
Q0302 – 003	17.8	3.286	4400–5000	258	12	31	32
Q0636 + 680	16.5	3.174	4300–4900	302	19	26	24
Q0956 + 122	17.8	3.301	4400–5000	242	18	30	29

Note. — For each quasar, the number of lines fitted and median  $b$  values are given for the indicated wavelength intervals in the observed frame. The number of lines fitted by the program is given for systems with column densities in excess of  $N_{\text{HI}} = 2 \times 10^{12} \text{ cm}^{-2}$  and  $N_{\text{HI}} = 3 \times 10^{14} \text{ cm}^{-2}$ . Median  $b$  values are given for the column density ranges  $N_{\text{HI}} = 3 \times 10^{12} - 3 \times 10^{13} \text{ cm}^{-2}$  and  $N_{\text{HI}} = 3 \times 10^{13} - 3 \times 10^{14} \text{ cm}^{-2}$ . Quasar magnitudes and emission-line redshifts are taken from Sargent *et al.* (1989).

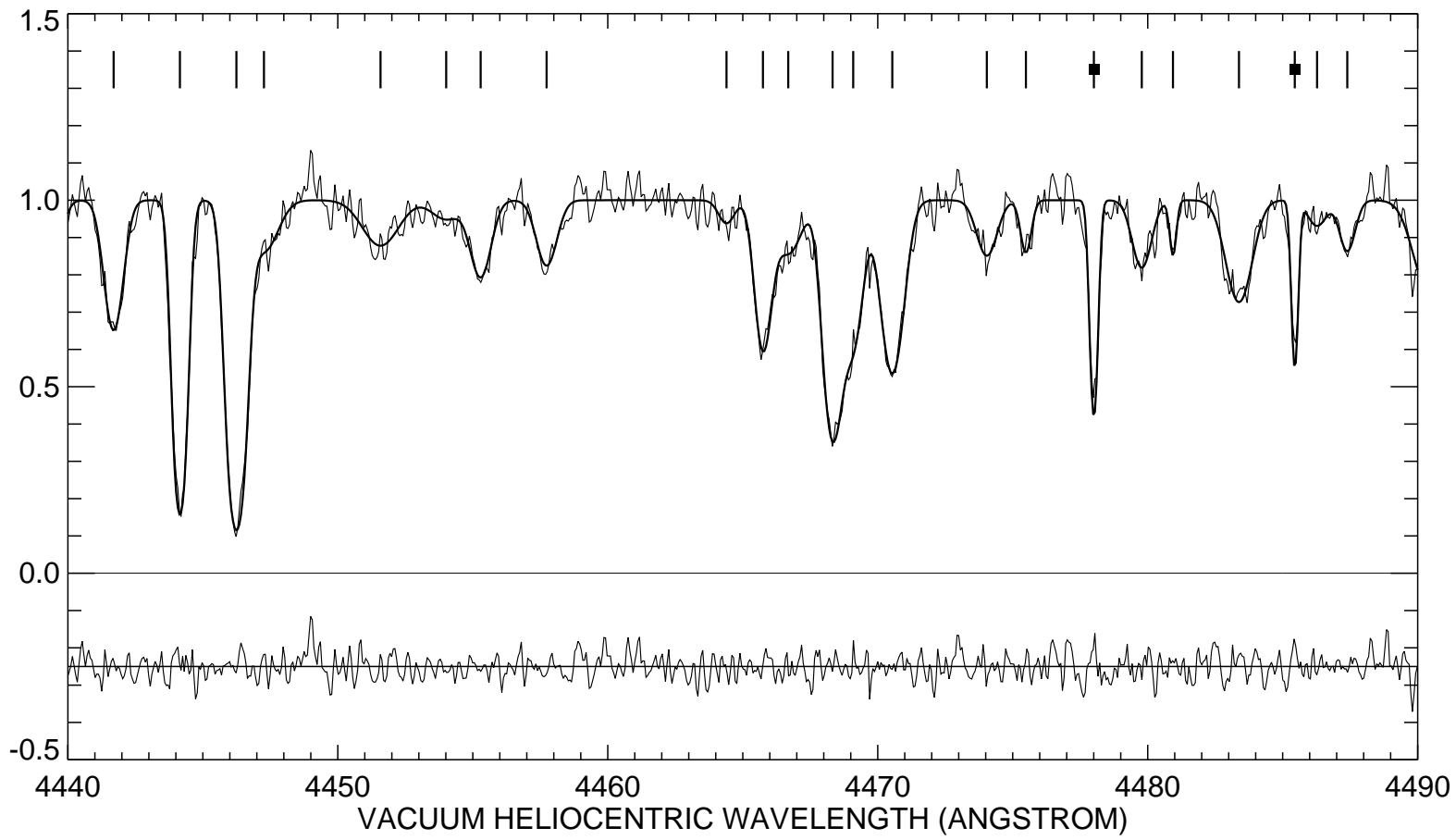
Table 2. Narrow Line Identifications

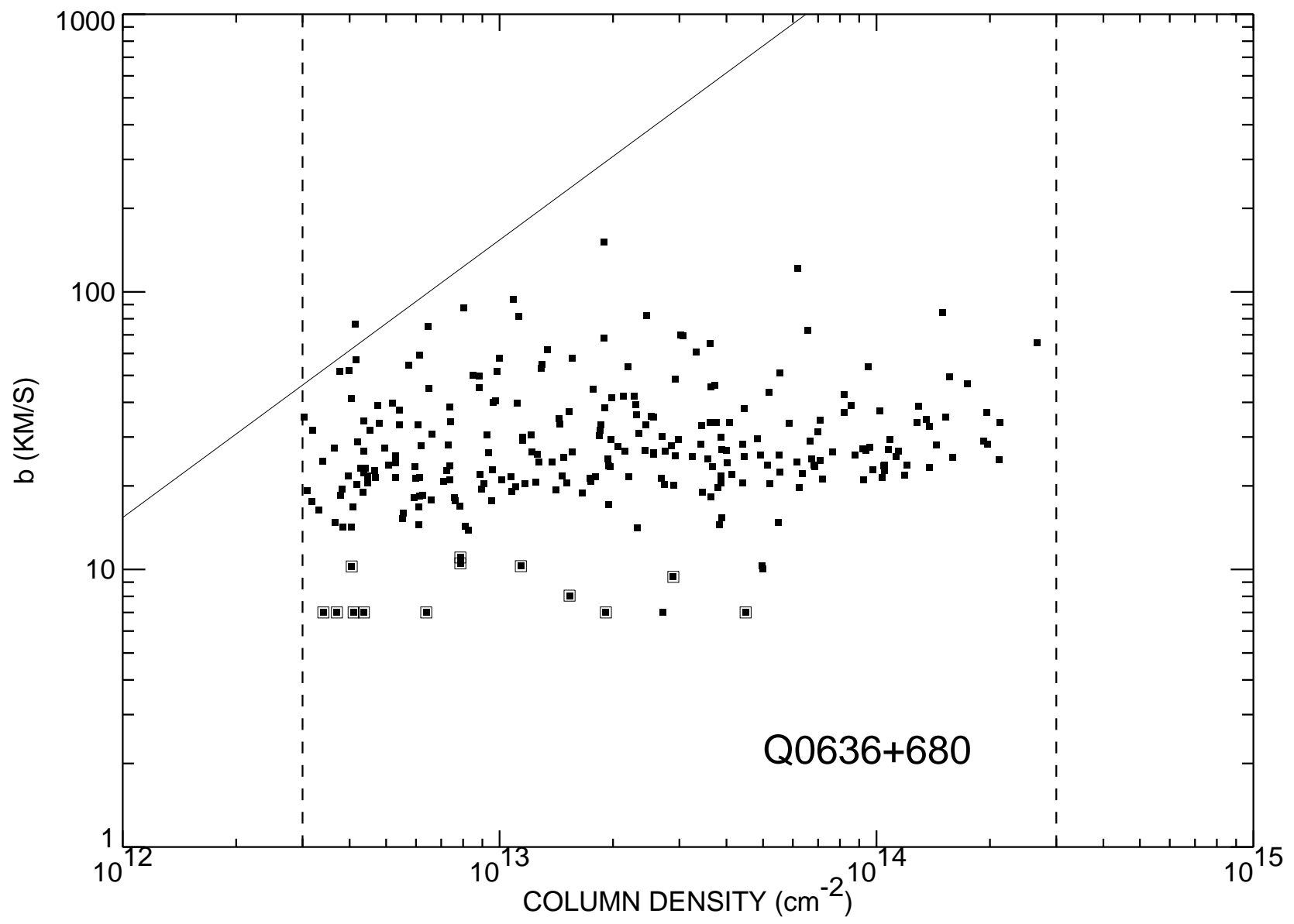
Quasar	$\lambda$ ( $\text{\AA}$ )	$b$ ( $\text{km s}^{-1}$ )	ID
Q0014 + 813	4538.65	9	C II (1334.5) 2.4009
	4582.39	10	—
	4597.20	7	—
Q0302 – 003	4478.01	13	C IV (1548.2) 1.8924
	4485.45	11	C IV (1550.8) 1.8924
	4832.47	14	Al II (1670.8) 1.8923
Q0636 + 680	4380.44	7	Si II (1260.4) 2.4754
	4390.19	14	—
	4417.85	2	C II (1334.5) 2.3104
	4494.69	10	C IV (1548.2) 1.9032
	4537.95	2	C IV (1548.2) 1.9311
	4545.47	7	C IV (1550.8) 1.9310
	4545.81	7	C IV (1550.8) 1.9313
	4637.98	3	C II (1334.5) 2.4754
	4642.63	10	—
	4646.95	11	Si III (1190.2) 2.9043
	4648.28	3	—
	4694.16	10	—
	4811.25	2	Mg II (2795.5) 0.7211
	4843.76	9	C IV (1548.2) 2.1287
	4848.16	10	C IV (1548.2) 2.1315
	4851.89	8	C IV (1550.8) 2.1287
	4856.22	11	C IV (1550.8) 2.1315
Q0956 + 122	4613.92	6	Si IV (1393.8) 2.3104
	4614.65	8	Si IV (1393.8) 2.3109
	4644.50	8	Si IV (1402.8) 2.3109
	4783.12	11	—
	4963.75	8	Si III (1206.5) 3.1141

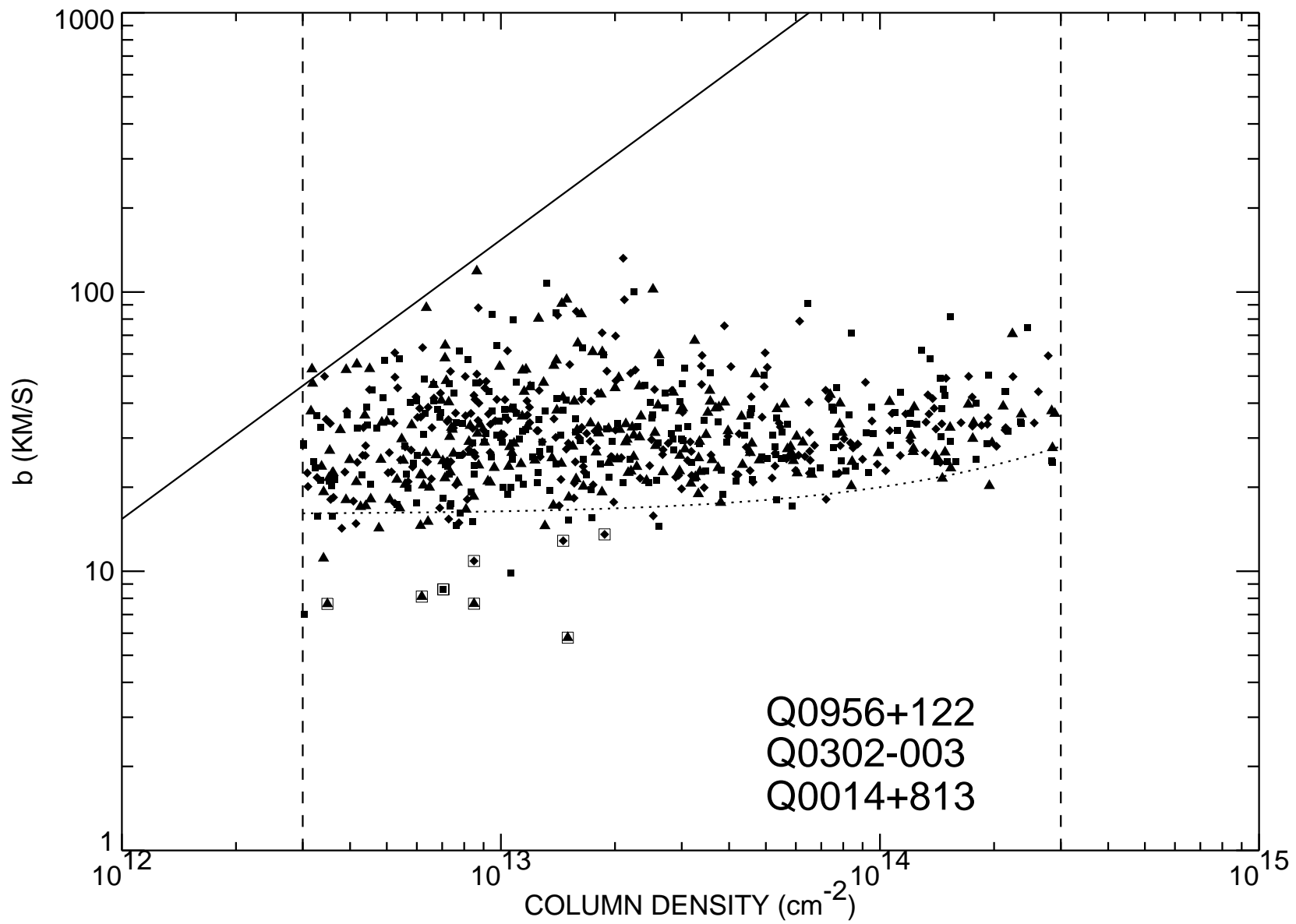


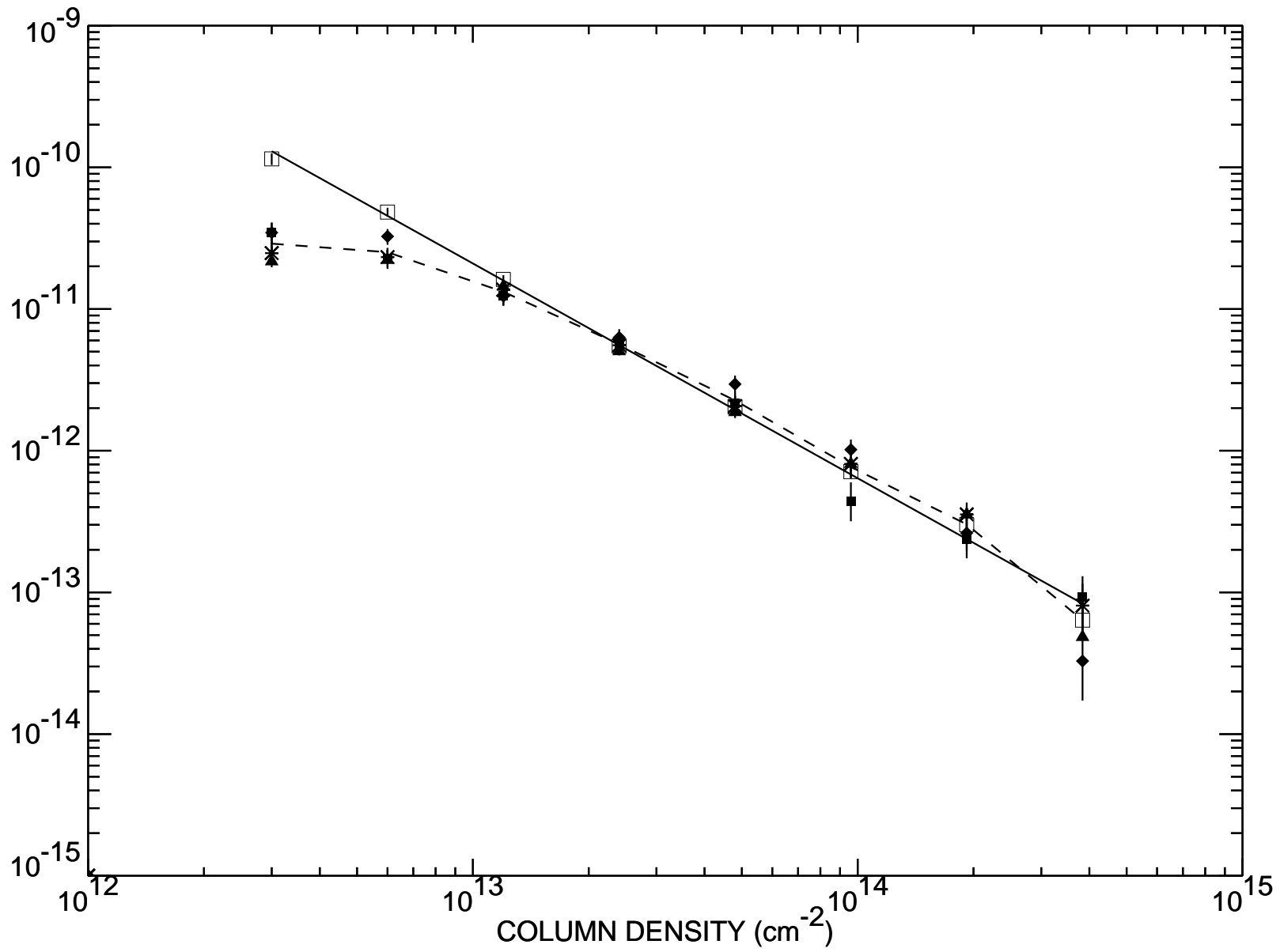
Table 3. Column Density Distribution

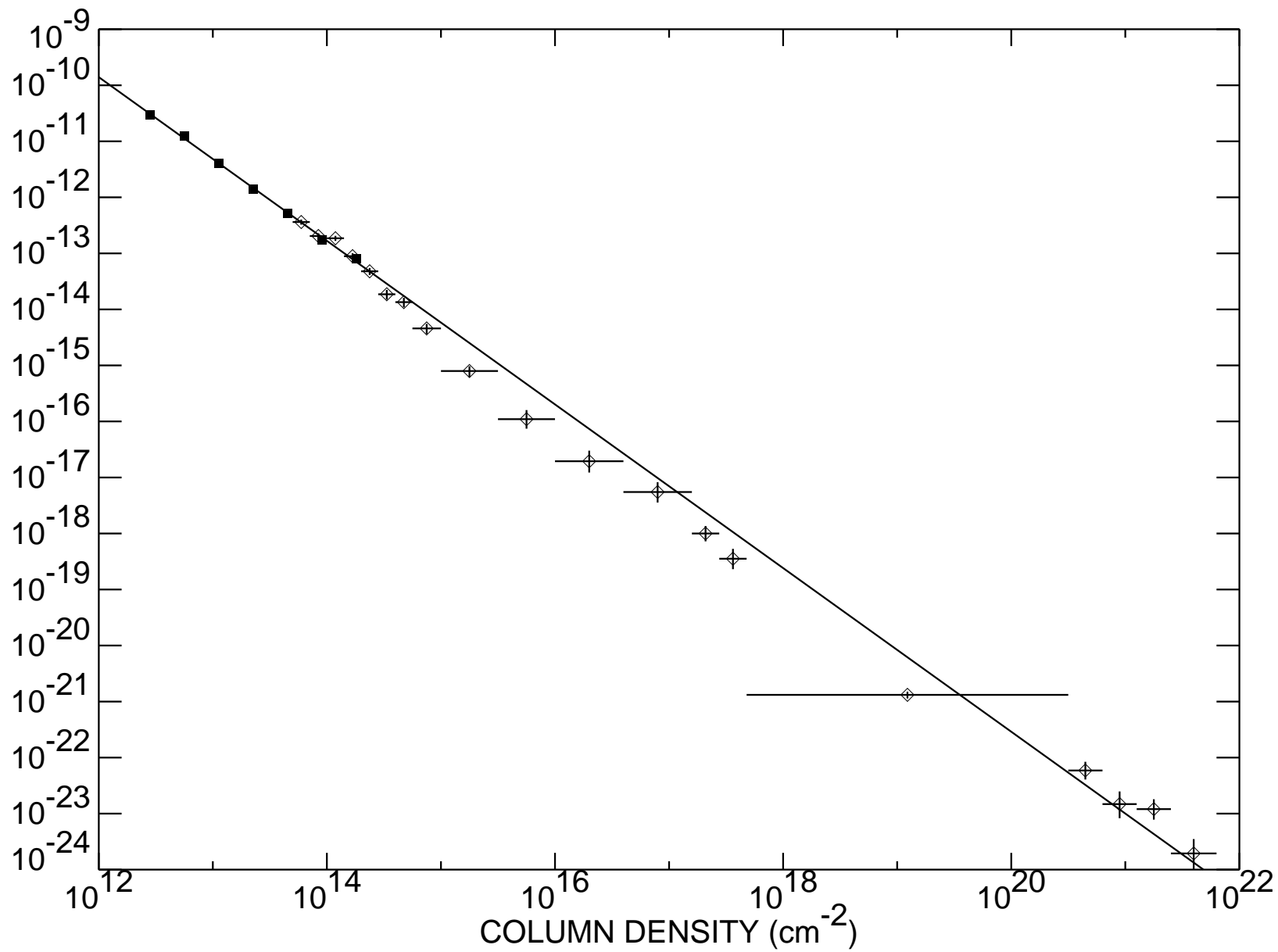
Log <sub>10</sub> N			
Range	Incompleteness	No. clouds	Log <sub>10</sub> $f(N)$
12.30–12.60	0.25	109	–10.53
12.60–12.90	0.52	188	–10.91
12.90–13.20	0.82	197	–11.39
13.20–13.51	1.03	173	–11.85
13.51–13.81	1.11	133	–12.29
13.81–14.11	1.08	88	–12.76
14.11–14.41	1.01	75	–13.10
> 14.41	1.0	77	—

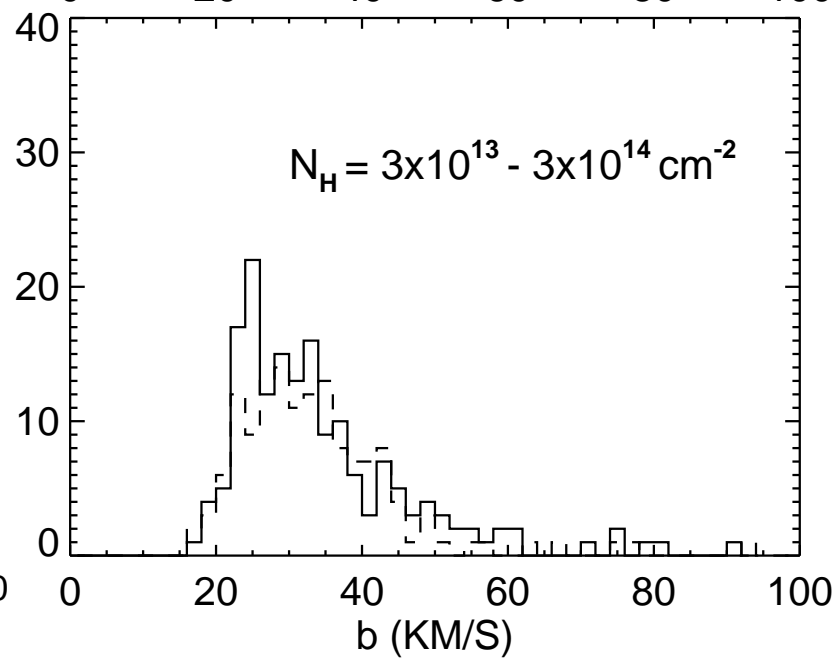
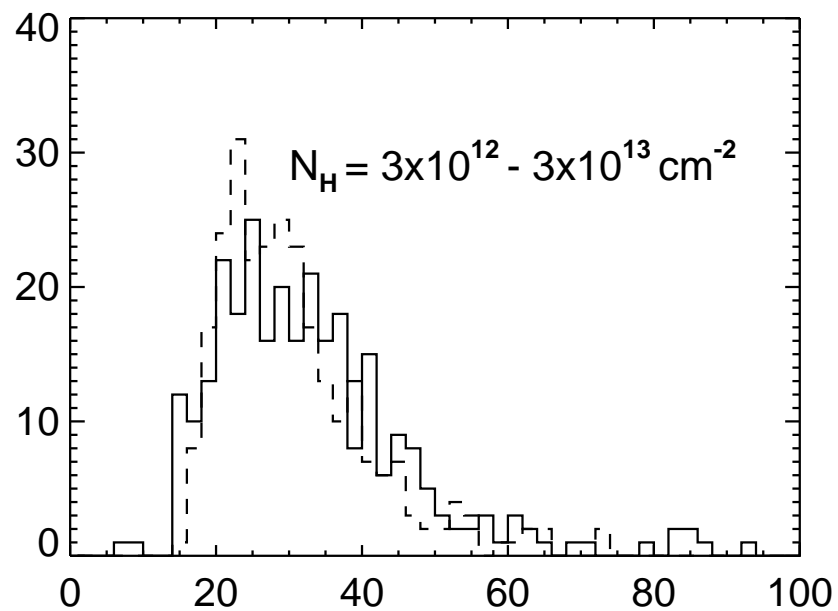
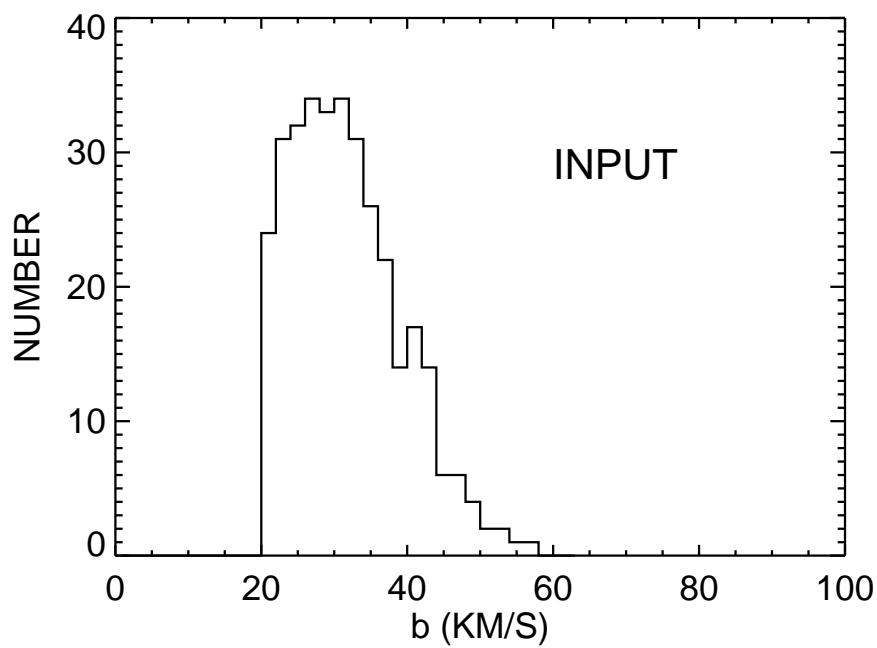


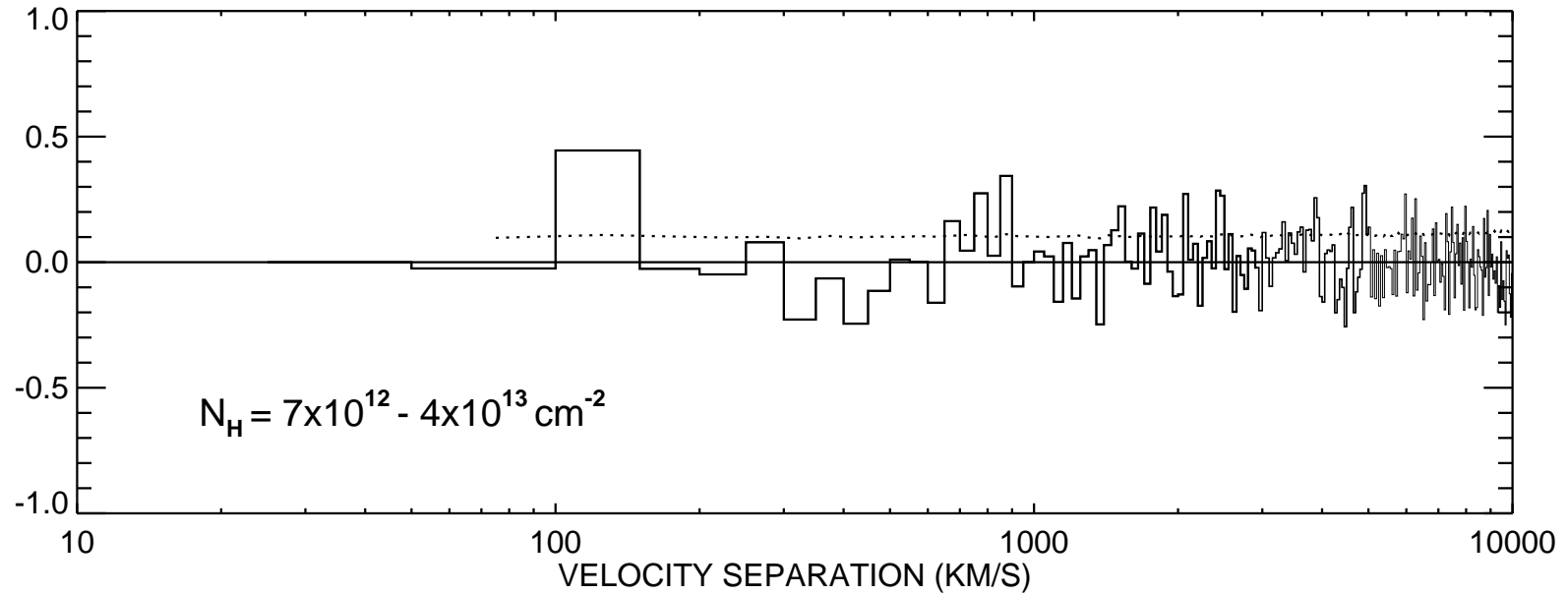
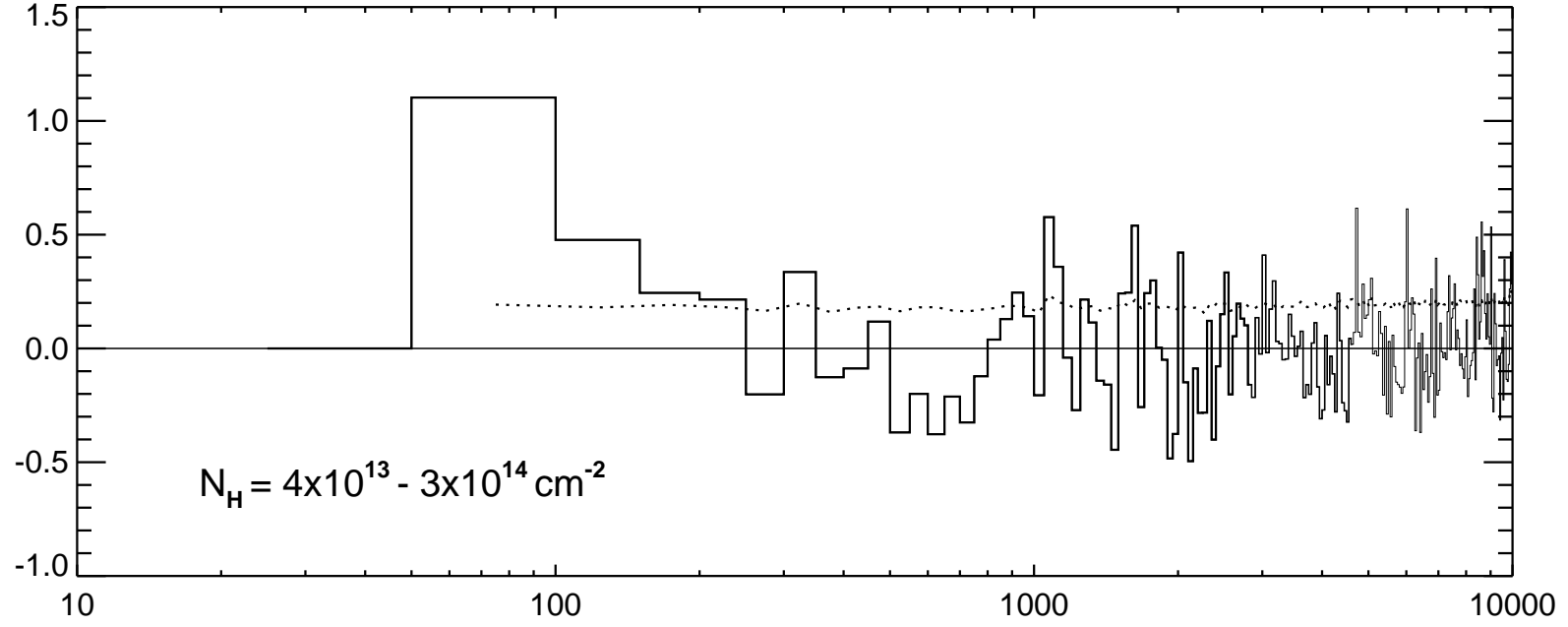












VELOCITY SEPARATION (KM/S)